Available online at www.sciencedirect.com
SCIENCE DIRECT®
International Journal of Heat and Mass Transfer 48 (2005) 361–371
International Journal of HEAT and MASS TRANSFER
www.elsevier.com/locate/ijhmt

Hierarchic modeling of heat transfer processes in heat exchangers

Andrej Horvat *,[1], Borut Mavko [2]

"Jožef Stefan" Institute, Reactor Engineering Division, Jamova 39, SI 1001, Ljubljana, Slovenia

Received 20 July 2004

Abstract

An alternate approach based on hierarchic modeling is proposed to simulate fluid and heat flow in heat exchangers. On the first level, the direct simulations have been performed for the geometry that is similar to a segment of the examined heat sink. Based on the obtained results, the Reynolds number dependencies of the scaling factors f and $StPr^{2/3}$ have been established. On the second level, the integral model of the whole heat sink has been built using the volume averaging technique (VAT). The averaging of the transport equations leads to a closure problem. The direct model Reynolds number dependencies f and $StPr^{2/3}$ have been used to calculate the local values of the drag coefficient $\widehat{C}_{\mathrm{d}}$ and the heat transfer coefficient $\widehat{\vartheta}$, which are needed in the integral model. The example calculations have been performed for 14 different pressure drops $\Delta\bar{p}$ across the aluminum heat sink. The whole-section drag coefficient $\overline{C}_{\mathrm{d}}$ and Nusselt number $\overline{Nu}$ have been calculated and compared with the experimental data [M. Rizzi, M. Canino, K. Hu, S. Jones, V. Travkin, I. Catton, Experimental investigation of pin fin heat sink effectiveness, in: Proc. of the 35th National Heat Transfer Conference Anaheim, California, 2001]. A good agreement between the modeling results and the experiment data has been reached with same discrepancies in the transitional regime. The constructed computational algorithm offers possibilities for geometry improvements and optimization, to achieve higher thermal effectiveness.

Keywords: Heat exchangers; Hierarchic modeling; Force convection; Conjugate heat transfer

1. Introduction

Heat exchangers are one of the basic industrial components and different variations of their form have been extensively studied (e.g. Žukauskas et al. [1], Kays and London [2], and Kakac [3]). In the past, the emphasis was on experimental work due to absence of today's computational power. The nature of experimental work enabled researchers to include in their studies only a few heat exchanger geometries, slightly varying geometry parameters. Furthermore, the flow conditions were limited by available experimental setups. Compared to

* Corresponding author. Tel.: +386 1 58 85 450; fax: +386 1 56 12 335.
E-mail addresses: andrej.horvat@ijs.si, andrej.horvat@ansys.com (A. Horvat), borut.mavko@ijs.si (B. Mavko).
[1] Currently at ANSYS Europe Ltd., The Gemini Building, Fermi Avenue, Harwell Int. Business Centre, Didcot, OX11 0QR, UK. Tel.: +44 1235 44 8067; fax: +44 1235 44 8001.
[2] Tel.: +386 1 58 85 450; fax: +386 1 56 12 335/258.

0017-9310/$ - see front matter © 2004 Elsevier Ltd. All rights reserved.
doi:10.1016/j.ijheatmasstransfer.2004.08.015

Nomenclature

A_f	$= V_f/l$, fluid flow cross-section
A_g	$= W \cdot L$, bottom surface
A_o	$= \pi dh$, wetted surface
A_{max}	$= l_{min}h$, cross-section with maximum velocity
c	specific heat
C_d	drag coefficient
d	diameter of pin-fins
d_h	$= 4V_f/A_o$, hydraulic diameter
dt	timestep
f	friction factor
G	mass flow rate
h	height of the pin-fins
H	height of the heat sink
H_b	height of the base plate
I_g	specific internal heat generation rate
l	pitch in the streamwise direction
l_{min}	minimum distance between two pin-fins (in the present case 45° to the stream direction)
L	length of the heat sink
N	number of numerical nodes in the direct model
Nu	Nusselt number
p	pressure
Pr	Prandtl number
Q	heat flow
Re	Reynolds number based on hydraulic diameter
S	$= A_o/V$, specific surface
St	Stanton number
T	temperature
T_0	initial temperature
T_g	temperature at bottom, $z = -H_b$ position
T_{if}	temperature at the fluid-base interface and the solid-base interface, $z = 0$ position
T_{in}	temperature at inflow, $x = 0$ position
T_{out}	temperature at outflow, $x = L$ position
u	velocity in the streamwise direction
v	velocity
v'	characteristic velocity scale of large eddies
v_{max}	velocity in the minimum cross-section (in the present case 45° to the stream direction)
V	volume
w	pitch in the horizontal spanwise direction
W	width of the heat sink
x	streamwise coordinate
y	horizontal spanwise coordinate
z	vertical spanwise coordinate

Greek symbols

α	volume fraction
η	Kolmogorov scale
λ	thermal diffusivity
μ	dynamic viscosity
ρ	density
ϑ	local heat transfer coefficient

Subscripts/superscripts

b	solid base-plate
f	fluid phase averaged variable
s	solid phase averaged variable
sf	solid–fluid interface
x	streamwise direction
y	horizontal spanwise direction
z	vertical spanwise direction

Symbols

$\bar{}$	whole-section values
$\hat{}$	integral model values
*	periodic residual part in the direct model

numerical analysis, these disadvantages of experimental work did not allow researchers to explore a wide range of parameters in order to find an optimal geometry. They rather limited the engineers' choice to well-tested and proven designs (Hesselgreaves [4]).

In the last 20 years, numerical approaches and methods, originally developed for the aerospace industry, have been increasingly employed to simulate processes in heat exchangers in order to find new designs for emerging technological needs. Pioneering work in the heat exchanger modeling was done in the late 70s by Meyder [5], Launder and Massey [6] and Antonopoulos [7], to name just a few, who performed two-dimensional simulations of fluid and heat flow in a segment of a heat exchanger using early RANS models. Today, due to extraordinary fast development of computer hardware, numerical simulations of a whole heat exchanger are already possible. Nevertheless, a question of turbulent flow simplifications remains an open issue. Namely, direct simulations of fluid and heat flow through a heat exchanger still cannot be performed, as the required computational resources are not available yet. Therefore, different turbulence models have to be applied to correctly predict fluid flow and heat transfer. In their recent work, Barsamian and Hassan [8] used a large-eddy simulation model to capture the turbulent part of the fluid motion.

In the present paper, authors propose an alternative approach based on hierarchic modeling in which the model and its computation are split onto two distinct

levels. On the first level, three-dimensional direct simulations of fluid and heat flow in a geometry similar to a heat exchanger segment are performed to study local thermo-hydraulic behavior. Based on the calculated three-dimensional velocity and temperature distributions, the local values of drag and heat transfer coefficients are determined. On the second level, an integral model, which uses the calculated local coefficients as input parameters, is applied to simulate heat transfer processes in a whole heat exchanger.

The use of the two-level hierarchic modeling approach has some clear advantages. Once local values of drag and heat transfer coefficients are calculated and mapped, generalized form of the integral model allows us to unify heat transfer calculation techniques for different kinds of heat exchangers and their structures. The case-specific geometrical arrangements, material properties and fluid flow conditions enter the integral calculation algorithm only as a series of precalculated coefficients. As these computational most demanding terms of momentum and heat exchange are determined on the separate level, the integral code is fast running, capable to accurately predict the heat flow for a whole heat exchanger in less than a minute.

In the present study, the described hierarchic modeling technique is applied to an electronic chip heat sink. The problem and therefore the motivation for current analysis is related to electronic chips' speed that is seriously limited by the thermal power they produce. As a consequence, electronic chips have to be intensively cooled using specially designed heat exchangers, submerged into air or water flow (Fabbri [9]). In our case the internal heat exchanging structure is made from high thermal conductive aluminum (Al) and exposed to air cross-flow.

The obtained simulation results are compared with the available experimental data (Rizzi et al. [10]). The comparison demonstrates the ability of the proposed hierarchic approach to reliably predict thermal conditions in heat exchangers.

2. Hierarchic modeling using two levels of models

To demonstrate principles of the hierarchic modeling approach, the geometry that was experimentally studied in the Morrin–Martinelli–Gier Memorial Heat Transfer Laboratory at University of California, Los Angeles (Rizzi et al. [10]) has been used. The general geometry arrangement of the heat sink is given in Fig. 1.

The length $\overline{L}$ and the width $\overline{W}$ of the heat sink are 11.43 cm (4.5″), whereas the height $\overline{H}$ is 3.81 cm (1.5″). The height of the conductive base plate, which connects pin-fins, is 0.635 cm (0.25″). The heat sink solid structure that is exposed to air cross-flow, consists of 31 rows of aluminum pin-fins in the streamwise (x-direction) and

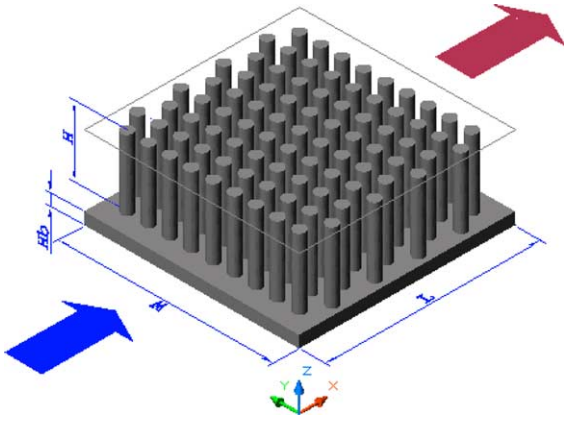

Fig. 1. Heat sink of an electronic chip—simulation domain of the integral model.

in the transverse direction (y-direction). The diameter of the pin-fins is $\hat{d} = 0.3175$ cm (0.125″). The pitch-to-diameter ratio in the streamwise direction $\hat{l}/\hat{d}$ is 1.06 and in the transverse direction $\hat{w}/\hat{d}$ is 2.12.

The material properties have been also taken from the considered experimental case. The heat sink was from the cast aluminum alloy 195. A uniform inlet flow profile has been assumed due to two rows of honeycomb flow-straighteners that were placed upstream the test section. The heat sink was heated from bellow by an electric resistance heater. A thermal isolation layer placed between the heater and the aluminum base had set the isothermal conditions at the base bottom.

2.1. Volume averaging technique (VAT)

It has been estimated that approximately 180 millions grid points would be needed to perform a direct simulation of the whole heat sink for the Reynolds numbers of interest. As the required number of grid points significantly exceeds our computational capabilities, an integral model has been built using the volume averaging technique (VAT) to model the whole heat exchanger. Applying VAT to the transport equations, the flow variables are averaged over a representative elementary volume (REV) of the heat sink. The averaged equations have a form of porous media flow equations, where each phase and its properties are separately defined over the whole simulation domain. The volume averaging procedure has been recently explained in detail by Horvat and Catton [11] and will not be repeated here. Nevertheless, it is important to note that applying VAT to the transport equations, the variations of smaller dimension than REV have to be modeled separately in a form of closure relations. These relations require knowledge of drag and heat transfer coefficients, which have been obtained from the direct simulations.

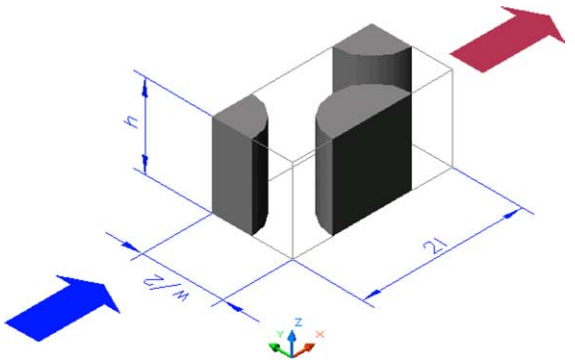

Fig. 2. Simulation domain of the direct model.

2.2. Scaling results between models

Kays and London [2] showed that momentum as well as heat transfer between fluid flow and a heat exchanger solid structure are similar for similar geometries at the same Reynolds number:

$$Re = 4\frac{G}{\mu_f}\left(\frac{l}{A_0}\right), \tag{1}$$

where G is a mass flow rate.

In addition to Reynolds number, they proposed a momentum-scaling factor:

$$f = 2\frac{\rho_f \Delta p}{G^2}\left(\frac{A_{max}^3}{A_0}\right), \tag{2}$$

and a thermal-scaling factor:

$$StPr^{2/3} = \frac{\vartheta A_{max}}{c_f G}\left(\frac{c_f \mu_f}{\lambda_f}\right)^{2/3} \tag{3}$$

as similarity variables. Considering these similarity variables, direct simulations can be performed for any similar geometry in order to scale the results to REV of the investigated heat sink.

In the present case, the direct simulations have been performed for one of geometries described in Kays and London [2] and shown in Fig. 2. Its width in the spanwise direction $w/2$ is 0.9525 cm (3/8″) and the length in the streamwise direction $2l$ is 1.905 cm (3/4″). With the pin-fin diameter d of 0.9525 cm (3/8″), the pitch-to-diameter ratio l/d is 1.0 and w/d is 2.0, respectively. The height h of the segment is 1.0 cm. The values of pitch-to-diameter ratio l/d and w/d are almost identical to the values $\hat{l}/\hat{d}$ and $\hat{w}/\hat{d}$ for the analyzed heat sink. Therefore, it is safe to assume momentum and heat flow conditions similar to those in REV of the heat sink.

3. Direct model

A separate model has been built to predict fluid and heat flow in the geometry (Fig. 2) similar to the heat sink REV. The CFX 5.5.1 commercial code has been used to perform time dependent numerical simulations on the level of the flow's Kolmogorov scale:

$$\frac{\eta}{l_{max}} = \left(\frac{\mu_f}{\rho_f v' l_{max}}\right)^{\frac{3}{4}}. \tag{4}$$

No additional turbulence model has been introduced into calculations. Following recommendations of Pope [15], an estimation has been made that the velocity fluctuations of energy containing eddies are $v' \sim 0.1 v_{max}$.

The basic transport equations (mass, momentum and thermal energy) that are incorporated in the CFX package are not repeated here as they can be found in any classical fluid dynamics book (e.g. Bird et al. [16]). However, it should be noted that in order for the direct model to correctly represent flow in the heat sink, periodicity has to be imposed on the transport equations in the streamwise direction.

3.1. Mass and momentum transport in the fluid flow

In the momentum transport equation, periodicity has been achieved by separating an average pressure drop Δp across the simulation domain from its residual part:

$$p = p^* - x\left(\frac{\Delta p}{2l}\right). \tag{5}$$

Thus, the momentum transport equation yields

$$\partial_t(\rho_f v_i) + \partial_j v_j(\rho_f v_i) = -\partial_j p^* \delta_{ij} + \partial_j(\mu_f \partial_j v_i) + \left(\frac{\Delta p}{2l}\right)\delta_{i,x}. \tag{6}$$

Referring to Fig. 2, the following boundary conditions for the fluid flow velocity have been assigned in the direct model:

$$\begin{aligned}
&(-l, y, z) \Longleftrightarrow (l, y, z) && \text{periodic boundary conditions,}\\
&(x, 0, z) && \text{symmetric boundary conditions,}\\
&(x, w/2, z) && \text{symmetric boundary conditions,}\\
&(x, y, 0) && \text{slip boundary conditions,}\\
&(x, y, h) && \text{slip boundary conditions,}\\
&(x_{sf}, y_{sf}, z) && \text{no-slip boundary conditions at the solid–fluid interface.}
\end{aligned} \tag{7}$$

The preset values of the pressure drop Δp across the simulation domain are summarized in Table 1. At initial simulation time, zero velocity field has been assigned.

3.2. Heat transport in the fluid flow

To model conjugate heat transfer between the fluid flow and the solid structure, an internal heat generation in the solid phase has been assumed as a source of ther-

Table 1
Pressure drop Δp (Pa), initial temperature $\overline{T}_0$ (°C) and solid phase heat generation rate I_g (W/cm^3) in the direct model calculations

Case	Δp (Pa)	$\overline{T}_0$ (°C)	I_g (W/cm^3)
1	0.04	23.0	0.2
2	0.08	23.0	0.2
3	0.16	23.0	0.2
4	0.32	23.0	0.2
5	0.64	23.0	0.2
6	1.28	23.0	0.2
7	1.50	23.0	0.2
8	2.00	23.0	0.2
9	2.56	23.0	0.2
10	5.12	23.0	0.2

mal energy. Periodicity of the temperature field has been introduced by subtracting an average temperature increase ΔT along the simulation domain:

$$T = T^* + x\left(\frac{\Delta T}{2l}\right), \quad \text{where} \quad \Delta T = \frac{I_g V_s}{c_f G}. \tag{8}$$

The energy transport equation changes its form to

$$\partial_t(\rho_f c_f T^*) + \partial_j v_j(\rho_f c_f T^*) = \partial_j(\lambda_f \partial_j T^*) - \rho_f c_f v_j\left(\frac{\Delta T}{2l}\right)\delta_{x,j}. \tag{9}$$

According to Eq. (8), the temperature increase ΔT depends on the internal heat generation rate I_g in the solid structure.

For the periodic part T^* of the fluid phase temperature, the following boundary conditions have been set:

$$\begin{aligned}
&(-l, y, z) \Longleftrightarrow (l, y, z) && \text{periodic boundary conditions,}\\
&(x, 0, z) && \text{symmetric boundary conditions,}\\
&(x, w/2, z) && \text{symmetric boundary conditions,}\\
&(x, y, 0) && \text{adiabatic boundary conditions,}\\
&(x, y, h) && \text{adiabatic boundary conditions,}\\
&(x_{sf}, y_{sf}, z) && \text{temperature and heat flux match at the solid–fluid interface.}
\end{aligned} \tag{10}$$

The preset values of the internal heat generation rate I_g in the solid phase are summarized in Table 1. For all simulations, the initial fluid temperature is set to $T_0 = 23\,°C$.

3.3. Heat transport in the structure

In a same way as in the fluid phase, the periodicity of the structure temperature field has been introduced by separating the average temperature increase ΔT from the temperature field T:

$$T = T^* + x\left(\frac{\Delta T}{2l}\right), \quad \text{where} \quad \Delta T = \frac{I_g V_s}{c_f G}. \tag{11}$$

Inserting Eq. (11) in the energy transport equation for the solid structure, the following form is obtained:

$$\partial_t(\rho_s, c_s T^*) = \partial_j(\lambda_s \partial_j T^*) + I_g. \tag{12}$$

For the periodic temperature T^*, the model boundary conditions have been prescribed as follows:

$$\begin{aligned}
&(-l, y, z) \Longleftrightarrow (l, y, z) && \text{periodic boundary conditions,}\\
&(x, 0, z) && \text{symmetric boundary conditions,}\\
&(x, w/2, z) && \text{symmetric boundary conditions,}\\
&(x, y, 0) && \text{adiabatic boundary conditions,}\\
&(x, y, h) && \text{adiabatic boundary conditions,}\\
&(x_{sf}, y_{sf}, z) && \text{temperature and heat flux match at the solid–fluid interface.}
\end{aligned} \tag{13}$$

The initial temperature of the solid structure has been set to the same initial temperature as the fluid phase: $T_0 = 23\,°C$.

4. Integral model of the heat sink

The integral model of the whole heat sinks is based on the volumetric averaging technique (VAT) that averages flow variable over a representative elementary volume (REV) of the heat sink. The derivation of volumetrically averaged transport equations is presented below in Sections 4.1–4.4. The integral model variables are marked with "^".

To solve the averaged form of transport equations with related boundary conditions, a separate numerical code has been constructed. The code, named POMIC (POrous Media Integral Code), is based on discretization principles of the finite volume method [12]. For a solver, the preconditioned conjugate gradient method [13] has been utilized. Further details on the code algorithm can be found in [14].

4.1. Mass and momentum transport in the fluid flow

In the integral model, the momentum transport equation has been developed using an additional assumption that the volume average velocity through the heat sink is unidirectional: $\hat{v} = \{\hat{u}, 0, 0\}$. As a consequence, the velocity varies only transversely to the flow direction. The pressure force across the entire simulation domain is in balance with shear forces and with drag that originates from the fluid–solid interaction. As a result, the momentum transport equation is reduced to

$$-\hat{\alpha}_f \mu_f(\partial_y \partial_y \hat{u}_f + \partial_z \partial_z \hat{u}_f) + \frac{1}{2}\widehat{C}_d \rho_f \hat{u}_f^2 \widehat{S} = \frac{\Delta \bar{p}}{\overline{L}}. \tag{14}$$

The boundary conditions for the integral model equations attempt to represent the experimental setup

Table 2
Pressure drop $\Delta\bar{p}$ (Pa) over the whole heat sink, inflow temperature $\overline{T}_{\mathrm{in}}$ (°C) and solid base bottom temperature $\overline{T}_{\mathrm{g}}$ (°C) in the integral model calculations

Case	$\Delta\bar{p}$ (Pa)	$\overline{T}_{\mathrm{in}}$ (°C)	$\overline{T}_{\mathrm{g}}$ (°C)
1	5.00	23.0	35.0
2	10.0	23.0	35.0
3	20.0	23.0	35.0
4	40.0	23.0	35.0
5	80.0	23.0	35.0
6	120.0	23.0	35.0
7	160.0	23.0	35.0
8	200.0	23.0	35.0
9	240.0	23.0	35.0
10	280.0	23.0	35.0
11	320.0	23.0	35.0
12	360.0	23.0	35.0
13	400.0	23.0	35.0
14	440.0	23.0	35.0

described previously in Section 2. For the momentum transport equation (14), no-slip boundary conditions have been implemented at all four walls parallel to the flow direction:

$$\hat{u}_{\mathrm{f}}(0,z)=0,\quad \hat{u}_{\mathrm{f}}(\overline{W},z)=0,\quad \hat{u}_{\mathrm{f}}(y,0)=0,\quad \hat{u}_{\mathrm{f}}(y,\overline{H})=0. \tag{15}$$

The preset values of the whole-section pressure drop $\Delta\bar{p}$ used in the calculations are summarized in Table 2.

4.2. Heat transport in the fluid flow

The energy transport equation for the fluid flow has also been developed using the unidirectional velocity assumption. The temperature field in the fluid results from a balance between thermal convection in the streamwise direction, thermal diffusion and the heat transferred from the solid structure to the fluid flow. Thus, a differential form of the energy equation for the fluid is

$$\hat{\alpha}_{\mathrm{f}}\rho_{\mathrm{f}}c_{\mathrm{f}}\hat{u}_{\mathrm{f}}\partial_x\widehat{T}_{\mathrm{f}}=\hat{\alpha}_{\mathrm{f}}\lambda_{\mathrm{f}}(\partial_x\partial_x\widehat{T}_{\mathrm{f}}+\partial_y\partial_y\widehat{T}_{\mathrm{f}}+\partial_z\partial_z\widehat{T}_{\mathrm{f}})-\hat{\vartheta}(\widehat{T}_{\mathrm{f}}-\widehat{T}_{\mathrm{s}})\widehat{S}. \tag{16}$$

For the fluid-phase energy transport equation (16), the simulation domain inflow and the bottom wall have been taken as isothermal:

$$\widehat{T}_{\mathrm{f}}(0,y,z)=\overline{T}_{\mathrm{in}},\quad \widehat{T}_{\mathrm{f}}(x,y,0)=\widehat{T}_{\mathrm{if}}(x,y,0), \tag{17}$$

whereas adiabatic boundary conditions have been prescribed assumed elsewhere:

$$\partial_x\widehat{T}_{\mathrm{f}}(\overline{L},y,z)=0,\quad \partial_y\widehat{T}_{\mathrm{f}}(x,0,z)=0,\quad \partial_y\widehat{T}_{\mathrm{f}}(x,\overline{W},z)=0,\quad \partial_z\widehat{T}_{\mathrm{f}}(x,y,\overline{H})=0. \tag{18}$$

The inflow boundary values $\overline{T}_{\mathrm{in}}$ of the fluid temperature $\widehat{T}_{\mathrm{f}}$ are summarized in Table 2. It has to be noted that the interface temperature $\widehat{T}_{\mathrm{if}}$ is influenced by a heat distribution in the conductive base-plate and is therefore position dependent.

4.3. Heat transport in the structure

The heat sink structure in each REV is not connected in the horizontal directions (Fig. 1). As a consequence, only thermal diffusion in the vertical direction is in balance with the heat leaving the structure through the fluid–solid interface, whereas thermal diffusion in the horizontal directions can be neglected. This simplifies the energy equation for the solid structure to

$$0=\hat{\alpha}_{\mathrm{s}},\lambda_{\mathrm{s}}\partial_z\partial_z\widehat{T}_{\mathrm{s}}+\hat{\vartheta}(\widehat{T}_{\mathrm{f}}-\widehat{T}_{\mathrm{s}})\widehat{S}. \tag{19}$$

For the solid-phase energy transport equation (19), the bottom wall has been prescribed as isothermal, whereas the top wall has been set as adiabatic:

$$\widehat{T}_{\mathrm{s}}(x,y,0)=\widehat{T}_{\mathrm{if}}(x,y,0),\quad \partial_z\widehat{T}_{\mathrm{s}}(x,y,\overline{H})=0. \tag{20}$$

4.4. Heat transport in the base-plate

In the solid base-plate, thermal diffusion is the only mechanism of heat transfer. As there is no heat transfer between the solid and the fluid phase, except at the upper boundary, the energy transport equation reduces to

$$0=\lambda_{\mathrm{s}}(\partial_x\partial_x\widehat{T}_{\mathrm{b}}+\partial_y\partial_y\widehat{T}_{\mathrm{b}}+\partial_z\partial_z\widehat{T}_{\mathrm{b}}). \tag{21}$$

The boundary conditions for the solid base-plate show the coupled nature of heat transfer between the fluid flow and the solid structure (Eqs. 16 and 19), and the base-plate (21). Namely, the heat flux between the fluid flow and the solid phase on one side, and the base-plate on the other side must be equal:

$$\lambda_{\mathrm{s}}\partial_z\widehat{T}_{\mathrm{b}}(x,y,0)=\hat{\alpha}_{\mathrm{f}}\lambda_{\mathrm{f}}\partial_z\widehat{T}_{\mathrm{f}}(x,y,0)+\hat{\alpha}_{\mathrm{s}}\lambda_{\mathrm{s}}\partial_z\widehat{T}_{\mathrm{s}}(x,y,0). \tag{22}$$

The calculated base temperature $\widehat{T}_{\mathrm{b}}$ at $(x,y,0)$, is equal to $\widehat{T}_{\mathrm{if}}$ which is used as the boundary condition (17) and (20) in the energy transport equations (16) and (19), respectively. At the bottom of the base-plate, isothermal boundary conditions have been prescribed:

$$\widehat{T}_{\mathrm{b}}(x,y,-\overline{H}_{\mathrm{b}})=\overline{T}_{\mathrm{g}}, \tag{23}$$

whereas the horizontal walls have been taken as adiabatic:

$$\partial_x\widehat{T}_{\mathrm{b}}(0,y,z)=0,\quad \partial_x\widehat{T}_{\mathrm{b}}(\overline{L},y,z)=0,\quad \partial_y\widehat{T}_{\mathrm{b}}(x,0,z)=0,\quad \partial_x\widehat{T}_{\mathrm{b}}(x,\overline{W},z)=0. \tag{24}$$

For the performed simulations, the bottom boundary values $\overline{T}_g$ of the base-plate temperature $\widehat{T}_b$ are summarized in Table 2.

5. Calculations and results

5.1. Direct model

First, the direct simulations of heat and fluid flow in the geometry (Fig. 2) similar to REV have been performed using the CFX 5.5.1 simulation program. The preset model parameters (pressure drop Δp, initial temperature T_0 and internal heat generation rate I_g) for each simulated case are summarized in Table 1. The numerical details of the simulations, like timestep and number of computational nodes, are given in Table 3.

Fig. 3 shows a qualitative representation of velocity v (left) and temperature T^* (right) in the fluid phase for the case 6, with the pressure drop Δp of 1.28 Pa imposed over the direct model simulation domain. The arrows in Fig. 3 (left) indicate the direction of the flow. Blue (dark) color of arrows denotes low velocity regions and red (light) color high velocity regions. The fluid temperature in Fig. 3 (right) is also represented by a color scale, where low temperature regions are blue (dark), and high temperature regions are red (light).

Table 3
Calculated Reynolds number Re, timestep dt (s) and number of node points N used in the direct model calculations

Case	Re	dt (s)	N
1	129	0.02	5769
2	210	0.01	5769
3	324	0.005	10,976
4	477	0.001	14,539
5	717	0.0005	31,904
6	931	0.0008	102,967
7	1031	0.0006	104,648
8	1222	0.0004	155,741
9	1408	0.0002	207,596
10	2083	0.0002	409,109

During direct simulations of fluid and heat flow, the fluid average velocity

$$u_f = \frac{1}{V_f}\int_{\widehat{V}_f} u\,dV, \tag{25}$$

the fluid average temperature

$$T_f^* = \frac{1}{u_f V_f}\int_{\widehat{V}_f} uT^*\,dV, \tag{26}$$

and the solid average temperature

$$T_s^* = \frac{1}{V_s}\int_{\widehat{V}_s} T^*\,dV, \tag{27}$$

were recorded at each timestep for further statistical evaluation. Simulations were terminated, when recorded values showed statistical equilibrium in turbulent flow (i.e. average values did not change for more than 1% over the next 100 records).

Average values and standard deviations of recorded velocity u_f, and temperatures T_f^* and T_s^* are presented in Fig. 4. It should be noted that the absolute values of velocity and temperatures are not important in this case, since the only purpose of the direct model is to calculate local drag and heat transfer coefficients for the integral model, $\widehat{C}_d$ and $\widehat{\vartheta}$. Namely, the correct values of local drag and heat transfer coefficients depend solely on relations between the pressure drop Δp, velocity u_f, and temperatures T_f^* and T_s^*.

Fig. 4 shows that the fluid average velocity u_f increases with the pressure drop Δp in a quadratic manner. As the solid average temperature T_s^* stays almost constant, the fluid average temperature T_f^* increases in a linear manner. Higher fluid temperatures T_f^* indicate that increasing velocity (or Reynolds number) intensifies mixing inside the fluid phase, which improves heat transfer from the solid to the fluid phase. Fig. 4 also reveals the transition to turbulence, which may be observed at pressure drop $\Delta p \sim 1.5$ Pa. The transition is evident by a sudden increase in the calculated standard deviations of the fluid average velocity u_f and temperature T_f^*.

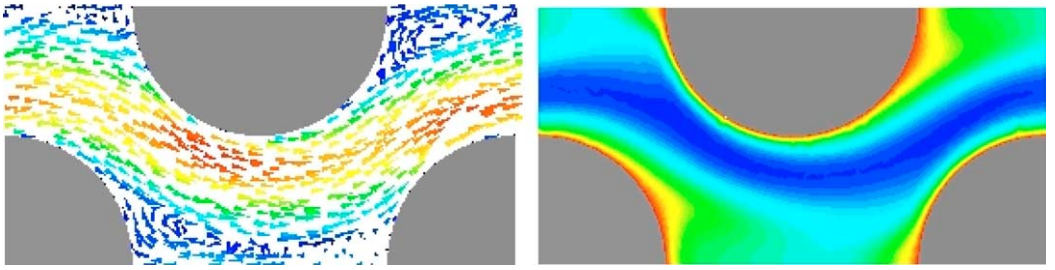

Fig. 3. Qualitative picture of the velocity field (left) and the temperature field in the fluid (right) calculated with the direct model for $\Delta p = 1.28$ Pa; case 6 in Table 1.

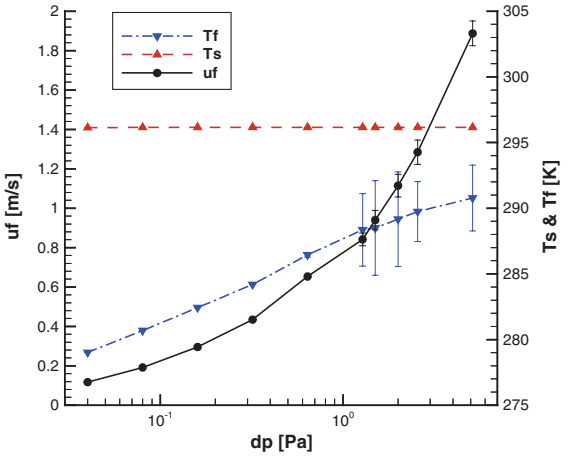

Fig. 4. Calculated fluid average velocity u_f (25), fluid average temperature T_f^* (26) and solid average temperature T_s^* (27) as functions of pressure drop Δp (Table 1).

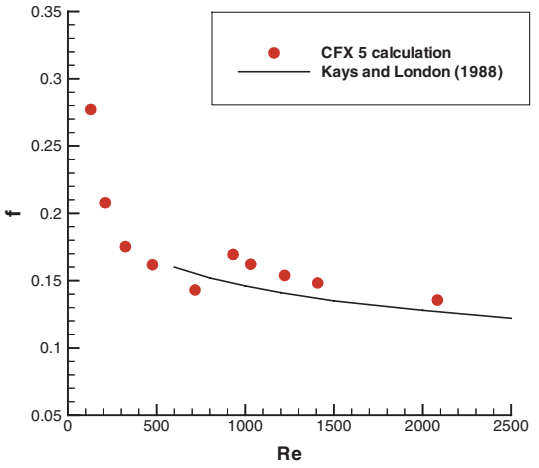

Fig. 5. Momentum scaling factor f as function of Reynolds number Re for the direct model.

The transition also changes the slope in the linear relation between the pressure drop Δp and the fluid average temperature T_f^*.

The similarity variables like Reynolds number Re, the momentum scaling factor f and the thermal scaling factor $StPr^{2/3}$ have been determined from the calculated values of the fluid average velocity u_f, the fluid average temperature T_f^* and the solid average temperature T_s^*. The expression for the Reynolds number

$$Re = \frac{\rho_f u_f d_h}{\mu_f} \tag{28}$$

is derived from (1) by introducing the relation $G = \rho_f u_f A_f$ and the definition for the hydraulic diameter $d_h = 4V_f/A_o$. Using the same expression for mass flow rate G, the momentum scaling factor (2) can be written as

$$f = 2\frac{\Delta p}{\rho_f u_f^2}\left(\frac{A_{max}^3}{A_o A_f^2}\right). \tag{29}$$

Furthermore, introducing the relations $\vartheta = I_g V_s/(T_s^* - T_f^*)A_o$, the thermal scaling factor (3) is transformed to

$$StPr^{2/3} = \frac{I_g}{c_f \rho_f u_f (T_s^* - T_f^*)}\left(\frac{A_{max} V_s}{A_f A_o}\right)\left(\frac{c_f \mu_f}{\lambda_f}\right)^{2/3}. \tag{30}$$

Fig. 5 shows the momentum scaling factor f as a function of Reynolds number Re in comparison with Kays and London data [2]. The agreement between the CFX results and the experimental data is good for the entire range of tested Reynolds numbers, although there is still room for improvement. The transition to turbulence at $Re \sim 800$ is expressed stronger than in the experimental results. It is believed that this is a consequence of the applied boundary conditions, which redirect the oscillations in a single plane, parallel to a boundary. Fig. 6 presents the calculated thermal scaling factor $StPr^{2/3}$ as a function of Reynolds number Re. The calculated results agree perfectly with the experimental data of Kays and London [2].

5.2. Scaling

Once the momentum scaling factor f (29) and the thermal scaling factor $StPr^{2/3}$ (30) have been determined as functions of Reynolds number Re from the direct model results (Figs. 5 and 6), one can calculate the local drag coefficient $\widehat{C}_d$ and the local heat transfer in the integral model. The local drag coefficient is expressed as

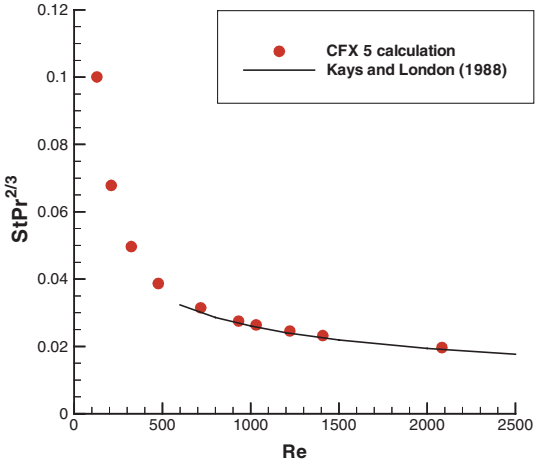

Fig. 6. Thermal scaling factor $StPr^{2/3}$ as function of Reynolds number Re for the direct model.

$$\widehat{C}_{\mathrm{d}} = f\left(\frac{\widehat{A}_{\mathrm{f}}^2 \widehat{V}}{\widehat{A}_{\max}^3 \hat{l}}\right), \tag{31}$$

where $\widehat{A}_{\mathrm{f}}$, $\widehat{V}$, $\widehat{A}_{\max}$ and $\hat{l}$ are geometrical parameters of the integral model REV. In a similar way, the local heat transfer coefficient for the integral model can be obtained from the thermal scaling factor $StPr^{2/3}$:

$$\hat{\vartheta} = (StPr^{2/3})\widehat{Re}Pr^{1/3}\left(\frac{\lambda_{\mathrm{f}}}{\hat{d}_{\mathrm{h}}}\right)\left(\frac{\widehat{A}_{\mathrm{f}}}{\widehat{A}_{\max}}\right). \tag{32}$$

5.3. Integral model

Using calculated distributions of the local drag coefficient $\widehat{C}_{\mathrm{d}}$ (31) and the local heat transfer coefficient $\hat{\vartheta}$ (32) as functions of local Reynolds number $\widehat{Re}$, the velocity and temperature fields have been calculated for the whole heat sink. The calculation parameters are given in Table 2.

As an example, Fig. 7 shows a cross-sectional view of the temperature field in the solid structure and in the base-plate for the case 9 (Table 2). Fig. 8 presents the temperature field in the airflow for the same case. The temperatures are in Celsius scale and the cross-sections are taken at the middle of the simulation domain, $\hat{y} = 0.5\overline{W}$. As may be observed in Fig. 8, the lowest temperatures in the airflow occur at the beginning of the heat sink (on the left side). The temperature raises as the air passes through the heat exchanging structure. Therefore, the highest temperatures in the airflow are expected at the exit (on the right side). The temperature field in the solid structure is more vertically stratified (Fig. 7), as the heat enters the structure from the bottom. Therefore, the lowest temperature in the solid phase is in the upper left corner and the highest at the bottom, in the base-plate. Figs. 7 and 8 demonstrate that, although the integral model is relatively crude, it can provide a detailed picture of heat transfer conditions in the heat sink.

To verify the results of the proposed two-level algorithm and to raise confidence in the hierarchic modeling

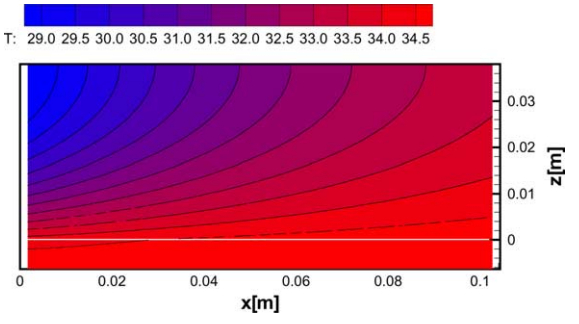

Fig. 7. Temperature in the solid structure and the base-plate ($\widehat{T}_{\mathrm{s}}$ and $\widehat{T}_{\mathrm{b}}$); case 9 in Table 2.

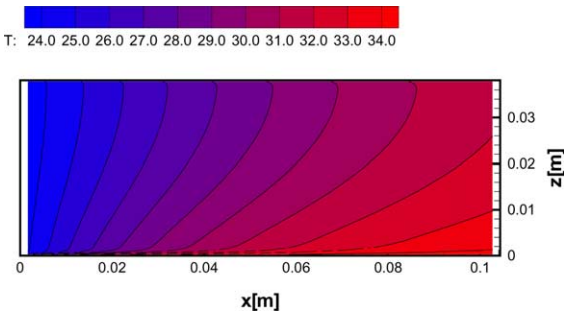

Fig. 8. Temperature field in the airflow ($\widehat{T}_{\mathrm{f}}$); case 9 in Table 2.

procedure, the whole-section drag coefficient $\overline{C}_{\mathrm{d}}$ and Nusselt number $\overline{Nu}$ have been calculated from the velocity and temperature fields of the integral model and compared to the available experimental results of Rizzi et al. [10]. The whole-section drag coefficient is calculated as

$$\overline{C}_{\mathrm{d}} = 2\frac{\Delta\bar{p}}{\rho_{\mathrm{f}}\bar{u}_{\mathrm{f}}^2}\left(\frac{\overline{V}}{\overline{A}_{\mathrm{o}}\overline{L}}\right), \tag{33}$$

and the whole-section Nusselt number as

$$\overline{Nu} = \frac{\overline{Q}\bar{d}_{\mathrm{h}}}{\lambda_{\mathrm{f}}(\overline{T}_{\mathrm{g}} - \overline{T}_{\mathrm{in}})\overline{A}_{\mathrm{g}}}, \tag{34}$$

where $\overline{Q} = \rho_{\mathrm{f}} c_{\mathrm{f}} \bar{u}_{\mathrm{f}}(\overline{T}_{\mathrm{out}} - \overline{T}_{\mathrm{in}})\overline{A}_{\mathrm{f}}$. The whole-section values of $\bar{u}_{\mathrm{f}}$, $\overline{T}_{\mathrm{in}}$ and $\overline{T}_{\mathrm{out}}$ are obtained with averaging of the integral model values $\hat{u}_{\mathrm{f}}$ and $\widehat{T}_{\mathrm{f}}$.

The results are presented in Figs. 9 and 10 as a function of whole-section Reynolds number that is defined as $\overline{Re} = \rho_{\mathrm{f}}\bar{u}_{\mathrm{f}}\bar{d}_{\mathrm{h}}/\mu_{\mathrm{f}}$. The comparison shows good agreement between the simulation results and the experimental data, which were taken at the lowest thermal power of

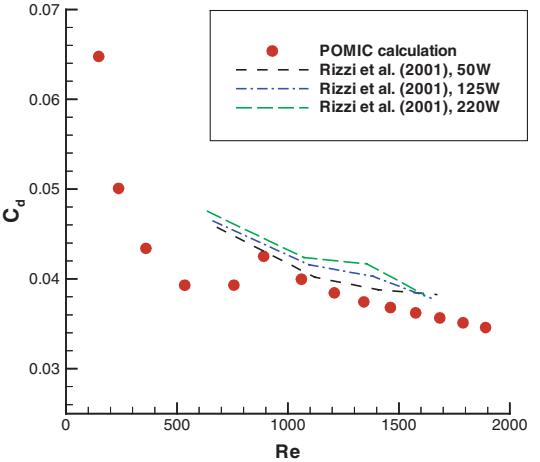

Fig. 9. Whole-section drag coefficient $\overline{C}_{\mathrm{d}}$ as function of Reynolds number $\overline{Re}$.

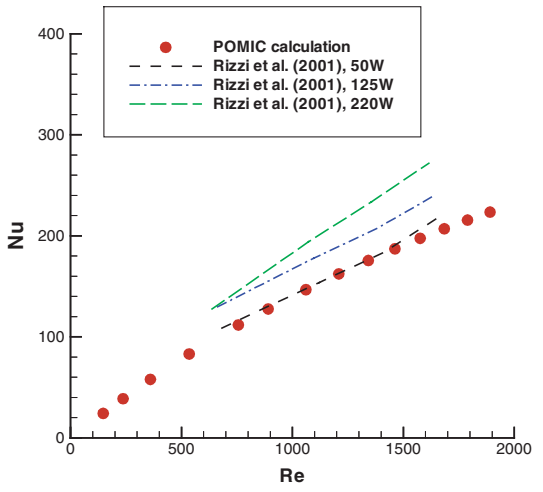

Fig. 10. Whole-section Nusselt number $\overline{Nu}$ as function of Reynolds number $\overline{Re}$.

50 W. As the buoyancy has not been included in our modeling procedure, the results show somewhat larger discrepancies at thermal power of 125 W and 220 W. This indicates that at higher power the additional effect of thermal stratification in the airflow becomes more important. Another issue that requires further attention is the transition region ($\overline{Re} \sim 800$). As shown in Fig. 9, the sudden increase in the calculated whole-section drag coefficient $\overline{C}_d$ is not confirmed by the experimental data. Nevertheless, the comparisons in Figs. 9 and 10 demonstrate that the hierarchic modeling procedure is able to provide reliable fluid and heat flow data in conjugate heat transfer situations.

6. Conclusions

The present paper describes an effort to develop a hierarchic modeling procedure for heat exchangers. As the direct simulation of fluid and heat flow in the whole heat exchanger would require currently unreachable computation resources, a technique has been developed and presented that splits the problem onto two levels.

It has been proposed that on the first level, the direct approach can be used to model processes in a representative elementary volume (REV) of a heat exchanger. Based on the direct simulation results for the geometry similar to REV, the momentum scaling factor f and the thermal scaling factor $StPr^{2/3}$ were obtained as functions of Reynolds number. These scaling factors were then used to obtain local values of the drag coefficient $\widehat{C}_d$ and the heat transfer coefficient $\hat{\vartheta}$ that are needed in the second level model.

In the present work, the hierarchic modeling procedure was demonstrated on an electronic chip heat sink for which first-hand experimental data were available [10]. The geometry for the first level model was taken from Kays and London [2]. In order to solve the system of transport equations with the prescribed boundary conditions, the pressure and temperature fields were transformed into the periodical form. The direct simulations of the periodic fluid and heat flow were performed with the CFX 5.5.1 software package.

On the second level, the integral model of the whole heat sink was built. For that purpose the volume averaging technique (VAT) was employed in order to model the heat sink cross-flow as porous media flow. As the averaging of transport equations leads to a closure problem, the local values of the drag coefficient $\widehat{C}_d$ and the heat transfer coefficient $\hat{\vartheta}$ were used to close the integral model equations. Based on the described procedure, the numerical program POMIC was built and then used for the heat sink calculations.

From the POMIC calculations, the temperature fields in the airflow and the solid structure were obtained. The calculated temperature fields demonstrate that the hierarchic modeling is able to predict local features of fluid and heat flow, although the details of the modeled flow were lost due to the averaging of transport equations on the second modeling level. The whole-section drag coefficient $\overline{C}_d$ and Nusselt number $\overline{Nu}$ were also determined as functions of Reynolds number and compared with the experimental data of Rizzi et al. [10] to verify the computational model and to validate the numerical code. The comparison showed a good agreement between the simulation results and the experimental data taken at the lowest thermal power (50 W), where stratification is not significant. Still, the numerical results display more distinctive drag coefficient increase in the transition region than the experimental data. This is believed to be a consequence of inadequate boundary conditions in the direct model.

The presented results demonstrate that the proposed hierarchic approach is an appropriate strategy for calculation of complex transport phenomena in heat exchanger where thermal conductivity of the solid structure has to be taken into account. The performed calculations also show that the developed two-level modeling algorithm is fast and it requires modest computational resources. Yet, it provides sufficiently accurate results to be applicable in future optimization calculations of heat exchanger morphologies.

Acknowledgments

A. Horvat gratefully acknowledges the financial support received from the Ministry of Education, Science and Sport of Republic of Slovenia under the project "Determination of morphological parameters for optimization of heat exchanger surfaces".

References

[1] A. Žukauskas, Convective heat transfer in cross flow, Handbook of Single-Phase Convective Heat Transfer, Wiley and Sons, New York, 1987.
[2] W.S. Kays, A.L. London, Compact Heat Exchangers, third ed., Krieger Publishing Company, Malabar, Florida, 1998.
[3] S. Kakac, Heat Exchangers: Thermo-Hydraulic Fundamentals and Design, second ed., Hemisphere Publishing, 1985.
[4] J.E. Hesselgreaves, Compact Heat Exchangers Selection, Design and Operation, Pergamon Press, 2001.
[5] R. Meyder, Solving the conservation equations in fuel rod bundles exposed to parallel flow by means of curvilinear-orthogonal coordinates, J. Comp. Phys. 17 (1975) 53–67.
[6] B.E. Launder, T.H. Massey, The numerical prediction of viscous flow and heat transfer in tube banks, J. Heat Transfer 100 (1978) 565–571.
[7] K.A. Antonopoulos, Prediction of flow and heat transfer in rod bundles, Ph.D. Thesis, Mechanical Engineering Department, Imperial College, London, UK, 1979.
[8] H.R. Barsamian, Y.A. Hassan, Large Eddy simulation of turbulent crossflow in tube bundles, Nucl. Eng. Des. J. 172 (1997) 103–122.
[9] G. Fabbri, Optimum performances of longitudinal convective fins with symmetrical and asymmetrical profiles, Int. J. Heat Fluid Flow 20 (1999) 634–641.
[10] M. Rizzi, M. Canino, K. Hu, S. Jones, V. Travkin, I. Catton, Experimental investigation of pin fin heat sink effectiveness, in: Proc. of the 35th National Heat Transfer Conference Anaheim, California, 2001.
[11] A. Horvat, I. Catton, Numerical technique for modeling conjugate heat transfer in an electronic device heat sink, Int. J. Heat Mass Transfer 46 (2003) 2155–2168.
[12] H.K. Versteeg, W. Malalasekera, An introduction to computational fluid dynamics, The Finite Volume Method, Prentice Hall, England, 1995, pp. 103–133.
[13] J.H. Ferziger, M. Perić, Computational method for fluid mechanics Chapter 5, Solution of Linear Equation Systems, Springer Verlag, Berlin, 1996, pp. 85–127.
[14] A. Horvat, Calculation of conjugate heat transfer in a heat sink using volume averaging technique (VAT), M.Sc. Thesis, University of California, Los Angeles, 2002.
[15] S.B. PopeTurbulent Flows, vol. 46, Cambridge University Press, 2000, pp. 152–155.
[16] R.B. Bird, W.E. Stewart, E.N. Lightfoot, Transport Phenomena, Wiley, New York, 1960.